

Composition-Triggered Growth of Monolayer $\text{MoTe}_{2(1-x)}\text{S}_{2x}$ Alloys with Coherent Phase Interfaces for High-Performance Broadband Photodetection

Xiaojian Wang, Meijie Zhu, Hui Pan, Xue Yang, Zeqi Hua, Shanshan Chen, Shaojuan Li, Haibo Shu, Jin Zhang,* and Qingliang Feng*

2D transitional metal dichalcogenides (TMDs) have attracted great interest for their advantageous application in room-temperature broadband photodetectors. Developing effective strategies to optimize the photo-carrier dynamical process of monolayer TMDs is still urgently necessary to extend wavelength range and reduce dark current due to the theoretical limitation of their intrinsic band structure. Herein, an interesting approach is reported to realize broadband photodetection from 532 to 1550 nm with low dark current for the first time by using composition-triggered growth of coherent atomic structures of enriched nanoscale mix-phase (2H/1T') monolayer $\text{MoTe}_{2(1-x)}\text{S}_{2x}$ alloys. The morphology and phase evolution at the nanoscale of monolayer $\text{MoTe}_{2(1-x)}\text{S}_{2x}$ alloys are elucidated as affected by tiny formation energy (ΔE) by the chemical composition of S/Te atoms triggered. As-grown enriched nanoscale mix-phase (2H/1T') of monolayer $\text{MoTe}_{2(1-x)}\text{S}_{2x}$ alloys devices exhibit typical n-type conductivity properties. More interestingly, the devices show an extended photo-response range from 532 to 1550 nm with reduced dark current to 10^{-10} A at 100 mV bias voltage. This work demonstrates that coherent atomic structure of enriched nanoscale mix-phase (2H/1T') monolayer TMDs alloys can be an alternative approach to obviously extend photo-response wavelength range without increasing dark current for room temperature broadband photodetection.

1. Introduction

Broadband photodetectors are widely used in optical communication, infrared guidance, and night vision due to their wide response from visible to short wave infrared range, and miniaturized integrated.^[1–6] The high mobility, direct bandgap, and tunable band structure of monolayer 2D transitional metal dichalcogenides (TMDs) make them great advantages for next-generation broadband photodetectors at room temperature, even high temperature.^[7–12] For example, the typical 2D semiconductor phase (2H) of MoS_2 and WSe_2 monolayers have shown high responsivity of 880 A W^{-1} ($\lambda = 561 \text{ nm}$) and fast photo-response of 23 ms ($\lambda = 650 \text{ nm}$), respectively.^[13,14] Meanwhile, the semi-metallic phase (1T') MoTe_2 could exhibit a broadband photo-response, but always with a high dark current or terrible noise ratio due to high conductivity of semi-metallic phase.^[15] Generally, it's almost impossible to fabricating broadband photodetectors by breakthrough in wavelength to short wave infrared range

X. Wang
College of Chemistry and Chemical Engineering
Lanzhou University
Lanzhou 730000, P. R. China


X. Wang, H. Pan, X. Yang, Q. Feng
School of Chemistry and Chemical Engineering
Key Laboratory of Special Functional and Smart Polymer Materials of
Ministry of Industry and Information Technology
Northwestern Polytechnical University
Xi'an 710072, P. R. China
E-mail: fengql@nwpu.edu.cn

M. Zhu, S. Chen
Department of Physics and Beijing Key Laboratory of Optoelectronic Functional Natural Materials and Micro-nano Devices
Renmin University of China
Beijing 100872, P. R. China

Z. Hua, H. Shu
College of Optical and Electronic Technology
China Jiliang University
Hangzhou 310018, P. R. China

S. Li
State Key Laboratory of Luminescence and Applications
Changchun Institute of Optics
Fine Mechanics and Physics
Chinese Academy of Sciences
Changchun 130033, P. R. China

J. Zhang
College of Chemistry and Molecular Engineering
Center for Nanochemistry
Beijing National Laboratory for Molecular Sciences
Peking University
Beijing 100871, P. R. China
E-mail: jinzhang@pku.edu.cn

 The ORCID identification number(s) for the author(s) of this article can be found under <https://doi.org/10.1002/adfm.202310066>

DOI: 10.1002/adfm.202310066

and low dark current concurrently by single intrinsic TMDs monolayer materials.

For now, TMDs-based broadband photodetectors have been reported by fabricating interlayer heterojunctions, interface engineering, or alloy engineering.^[16–20] First, the optical absorption and photo-carrier dynamics of heterostructures can be well tuned by band alignment mechanism, such as graphene/MoTe₂/Si heterojunction exhibits a response spectrum spanning from 300 to 1800 nm with dark current $\approx 10^{-12}$ A at zero bias voltage.^[21] Moreover, the ferroelectric polarization gating could be utilized to regulating charge trapping, transfer, and recombination, and extend the response wavelength range finally.^[22] For example, PVDF/MoS₂ based photodetectors shown an extended wavelength range from 0.5 to 1.55 μm with dark current $\approx 10^{-11}$ A at 100 mV bias voltage.^[23] Inevitably, the complicated fabricating process of heterojunction makes more technical challenge and cost for industrial production.^[24–26] On the other hand, alloying engineering of 2D TMDs are widely used to tune band structure of themselves.^[27–30] For monolayer TMDs alloy with similar phase, such as 2H phase of Monolayer MoS₂xSe_{2(1-x)} alloys possess a continuously adjustable bandgap, ranging from semiconducting MoS₂ monolayers with bandgap of 1.86 eV to semiconducting MoSe₂ monolayers of 1.55 eV.^[31,32] As a result, the value of bandgap range is limited by two-end point of 2H semiconductors, which is almost impossible extend to short wave infrared region. And for the alloying of different phase TMDs, take monolayer WSe_{2(1-x)}Te_{2x} alloys as an example, the bandgap can be continuously tuned from 1.67 to 1.44 eV with semiconducting H-phase when the chemical composition of Te < 0.45.^[33] Interestingly, the bandgap tunes to 0 eV suddenly when the phase of alloy transition to 1T', which is also be semi-metallic, no matter how many contents of Te in monolayer alloys. Hence, fabricating H-T' phase of inner layer heterojunctions would be alternative strategy to optimizing dark current and extending wavelength range by combing each advantage.

Herein, we synthesized enriched nanoscale mix-phase (2H/1T') MoTe_{2(1-x)}S_{2x} alloy monolayers with coherent atomic structures by modified chemical vapor deposition (CVD) to broaden absorption wavelength range with low dark current and fast photo-response time. The phase transition state of coherent atomic structures from 2H to 1T' are observed in CVD-grown mix-phase alloys by using atomic-resolution annular dark field scanning transmission electron microscopy (ADF-STEM). The morphology and phase evolution of nanoscale mix-phase MoTe_{2(1-x)}S_{2x} alloys in composition-triggered growth are elucidated with the view of formation energy of crystalline structure by density functional theory (DFT) calculations. Large area of enriched nanoscale mix-phase MoTe_{2(1-x)}S_{2x} alloy monolayers with coherent atomic structures are further confirmed by Raman mapping, angle-resolved polarized optical microscopy (ARPOM), and X-ray photoelectron spectroscopy (XPS). Electrical transport and photo-response measurements of MoTe_{2(1-x)}S_{2x} alloys based devices demonstrated that the carrier type and photo-response wavelength range can be systematically tuned by adjusting the alloy composition. Especially, mix-phase MoTe_{2(1-x)}S_{2x} alloy exhibits a broadband photo-response from 532 to 1550 nm while still maintaining a low dark current and even a faster response time. Our work provides a new approach to extend wavelength range and reduce dark current for high-performance broadband

photodetectors by the nanoscale mix-phase engineering of 2H/1T' TMDs alloy materials.

2. Results and Discussion

As shown in **Figure 1a**, sulfur (S), Tellurium (Te), and molybdenum trioxide (MoO₃) powder are placed in three quartz boats with temperatures of $T_S \approx 200$ °C, $T_{Te} \approx 500$ °C, and $T_{Mo} \approx 800$ °C, respectively. SiO₂/Si substrate is placed on the quartz boat, and MoO₃ and NaCl powders are mixed and put in quartz boat. The phase and chemical composition of monolayer MoTe_{2(1-x)}S_{2x} alloy are controlled by adjusting S/Te ratio (more details see Experimental Section). Figures S1 and S2 (Supporting Information) show structural characterizations of the synthesized samples. The results show that regulation of the composition causes the monolayer MoTe_{2(1-x)}S_{2x} alloy undergo the phase transition. In our recent works, ARPOM can be utilized for nondestructive identification of grain boundaries and orientation in 1T' TMDs.^[34,35] **Figure 1b–d** exhibit ARPOM images of Te-rich, mid-composition, and S-rich alloys, respectively. ARPOM images of MoTe_{2(1-x)}S_{2x} alloys with different compositions exhibit significantly variable optical contrast. **Figure 1e–g** exhibit polar plots of optical contrast as a function of polarization angle for Te-rich, mid-composition, and S-rich alloys (**Figure S3**, Supporting Information shows the original ARPOM images). The polar plots of Te-rich alloys for marked regions 1 and 2 both exhibit high polarization ratios, while the values of the polarization ratio for S-rich alloys are almost 1. For mid-composition alloys, the polarization ratio of marked region 1 is significantly higher than region 2 (The value of polarization ratio for region 2 is almost 1), which demonstrates that marked region 1 is 1T' phase alloy, and the region 2 is 2H phase alloy. Those results are further supported by Raman spectra of monolayer Te-rich, mid-composition, and S-rich alloys as shown in **Figure 1h–j**, respectively. For Te-rich alloy, the peaks ≈ 160.6 , 266.6, 327.4, and 395.3 cm^{-1} correspond to Raman modes of 1T' MoTe₂-A_g-like, 1T' MoTe₂-A_g-like, 1T' MoS₂-J₃-like and 1T' MoS₂-A_{1g}-like, respectively (**Figure 1h**). In Raman spectra of region 1 for mid-composition alloy, the peaks ≈ 163.6 , 230.1, 255.8, 353.8, and 396.6 cm^{-1} correspond to Raman modes of 1T' MoTe₂-A_g-like, 2H MoTe₂-E_{2g}-like, 1T' MoTe₂-A_g-like, 2H MoS₂-E¹_{2g}-like and 2H MoS₂-A_{1g}-like, respectively (**Figure 1i**). For mid-composition alloy at region 2, four different peaks at 233.7, 253.2, 365.6, and 398.1 cm^{-1} correspond to 2H MoTe₂-E_{2g}-like, 1T' MoTe₂-A_g-like, 2H MoS₂-E¹_{2g}-like and 2H MoS₂-A_{1g}-like Raman modes, respectively (**Figure 1i**). For S-rich alloy, the Raman modes of 2H MoTe₂-E_{2g}-like, 2H MoS₂-E¹_{2g}-like and 2H MoS₂-A_{1g}-like are observed at 240.3, 377.4, and 401.2 cm^{-1} , respectively (**Figure 1j**). Therefore, Te-rich and S-rich alloys are homogeneous 1T' and 2H phases, respectively, while mid-composition alloy is a mix-phase.

The atomic structures of monolayer MoTe_{2(1-x)}S_{2x} alloys are investigated by using ADF-STEM imaging. **Figure 2a** shows the colored ADF-STEM image of the mix-phase MoTe_{2(1-x)}S_{2x} alloy. The original ADF-STEM image is shown in **Figure S4** (Supporting Information). As the ADF contrast is proportional to atomic number (Z), the brightness of S₁ sites in Z-contrast imaging (ADF-STEM imaging) is much dimmer than that of Te and Mo sites ($Z_S = 16$, $Z_{Te} = 52$ and $Z_{Mo} = 42$). **Figure S5** (Supporting Information) shows the zoomed-in STEM images of different

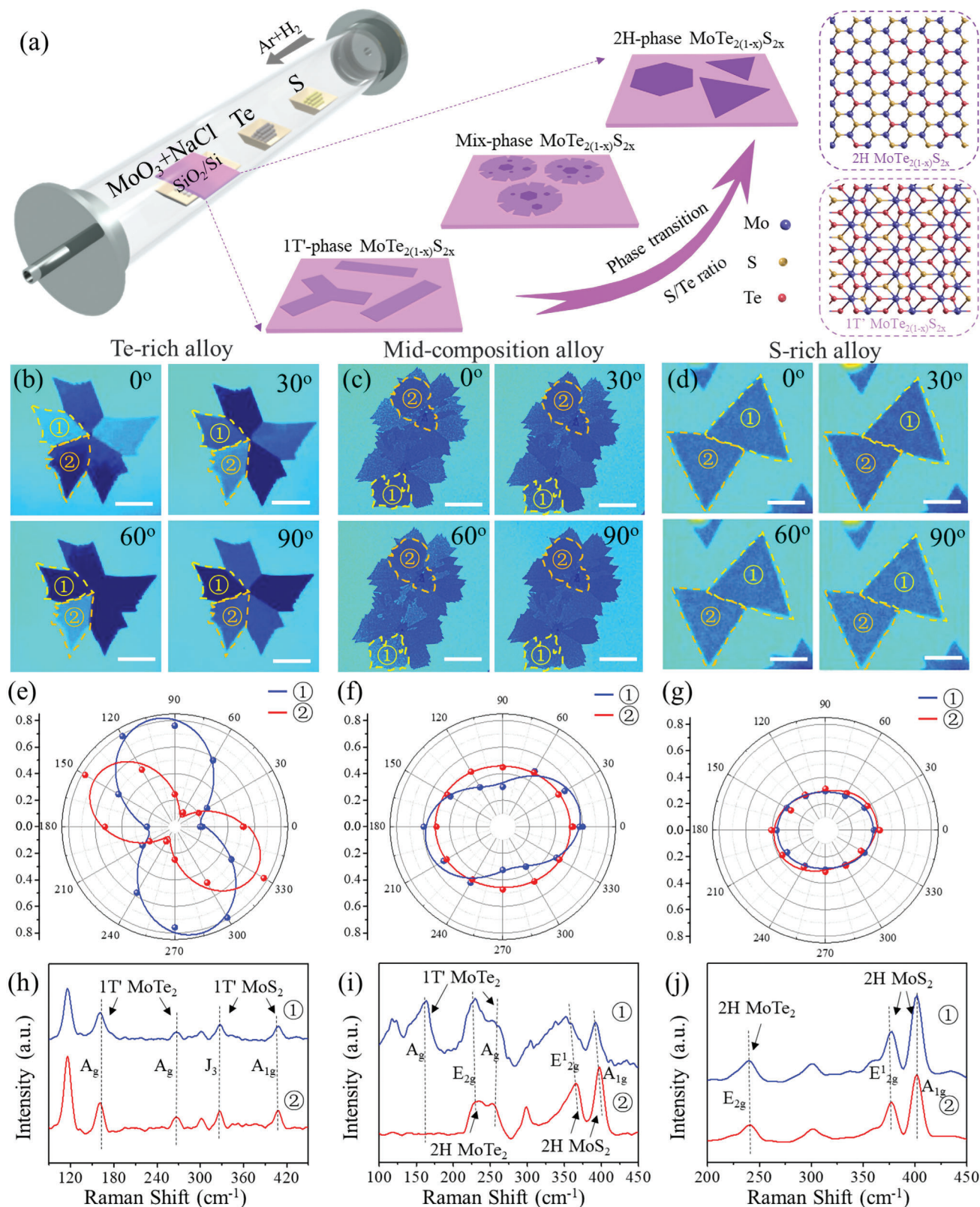


Figure 1. Controlled growth of $\text{MoTe}_{2(1-x)}\text{S}_{2x}$ alloys. a) Schematic representation of the experimental setup and mechanism for synthesis of $\text{MoTe}_{2(1-x)}\text{S}_{2x}$ alloy. b–d) ARPOM images for various polarization angles of Te-rich, mid-composition, and S-rich alloys, respectively. e–g) Polar plots of optical contrast with polarization angle for regions 1 and 2 of Te-rich, mid-composition, and S-rich alloys in (b), (c), and (d), respectively. h–j) Raman spectra for regions 1 and 2 of Te-rich, mid-composition, and S-rich alloys in (b), (c), and (d), respectively.

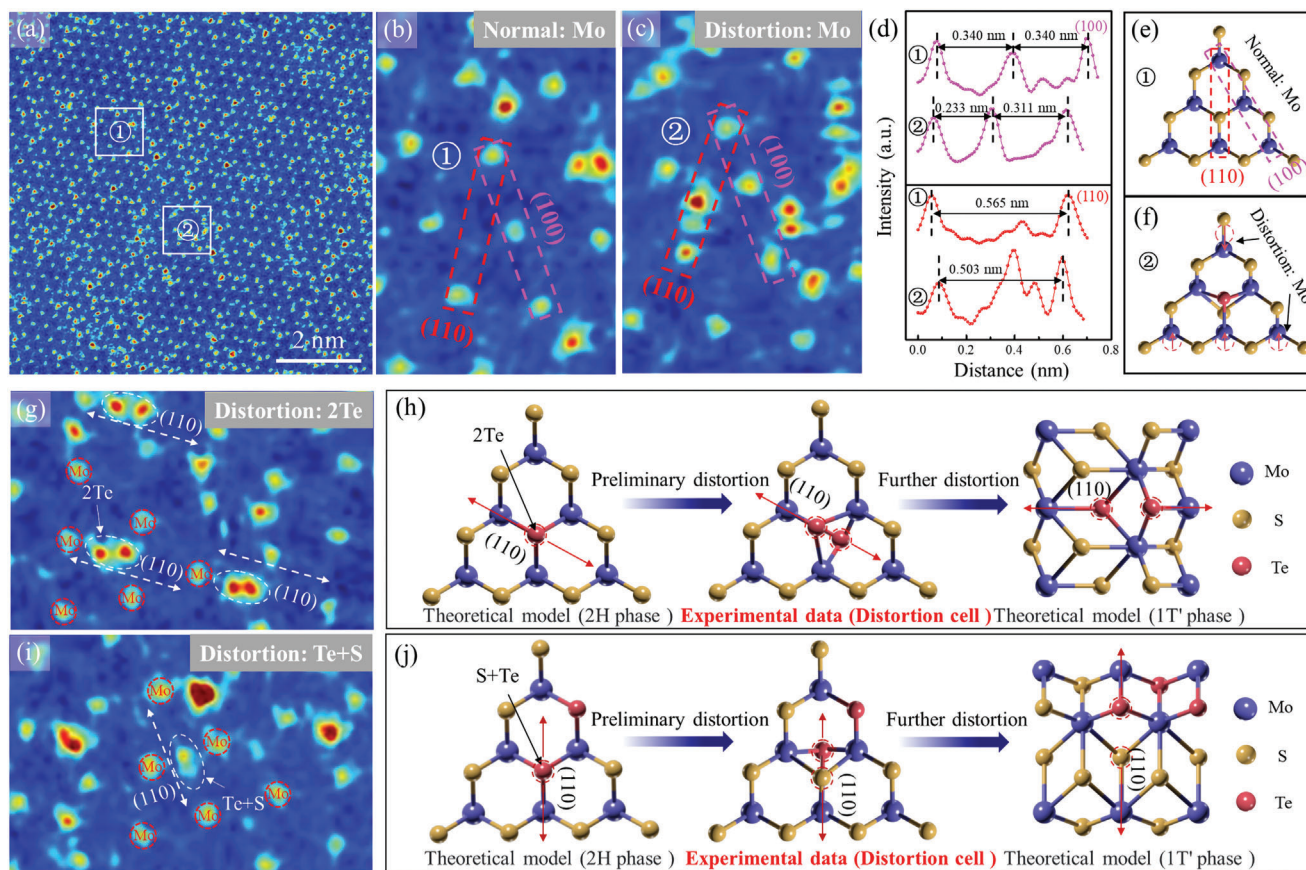


Figure 2. STEM-ADF analysis of coherent atomic structure in monolayer mix-phase $\text{MoTe}_{2(1-x)}\text{S}_{2x}$ alloys. a) Colored ADF-STEM images of mix-phase $\text{MoTe}_{2(1-x)}\text{S}_{2x}$. b,c) The zoomed-in images of regions 1 (normal: Mo) and 2 (distortion: Mo) in (a), respectively. d) Intensity line profiles along with (110) and (100) in (b) and (c). e,f) Atomic models of normal and distorted structures in (b) and (c), respectively. g,i) Colored ADF-STEM images of distorted structures of 2Te and Te+S coordination in monolayer mix-phase $\text{MoTe}_{2(1-x)}\text{S}_{2x}$ alloy, respectively. h,j) Schematic diagrams of atomic model for the evolution of 2Te and Te+S sites distorted structures, respectively.

regions of mix-phase $\text{MoTe}_{2(1-x)}\text{S}_{2x}$ alloy, and the marked circle areas are S or Te vacancy defects. Interestingly, the distorted atomic structure in monolayer mix-phase $\text{MoTe}_{2(1-x)}\text{S}_{2x}$ alloy are observed that differs from normal H-phase or T'-phase. Figures S6 and S7 (Supporting Information) show ADF-STEM images of normal and distorted coordination atoms for 2Te and Te+S sites in monolayer mix-phase $\text{MoTe}_{2(1-x)}\text{S}_{2x}$ alloy. Figure 2b,c are zoomed-in images of marked region 1 and 2 in Figure 2a, respectively. Region 1 has normal Mo sites along with (110) and (100) orientation, while both Mo sites in region 2 are shifted. The difference in interatomic distances of Mo sites between regions 1 and 2 is further verified by corresponding intensity line profile shown in Figure 2d. The distances between three Mo atoms along with (100) orientation of distorted structure exhibit one narrow and one wide peaks, similar with 1T' phase structure. The atomic models shown in Figure 2e,f reveal the process of distortion from normal structure to distorted one. The 2H-phase TMDs exhibit three equivalent (110) orientations due to their threefold symmetry crystal structure (Figure S8, Supporting Information). Figure 2g–i and Figure S9 (Supporting Information) show STEM images of distorted structures of 2Te and Te+S sites in monolayer mix-phase $\text{MoTe}_{2(1-x)}\text{S}_{2x}$ alloy. The 2Te/Te+S atoms are displaced along with (110) orientations in mix-phase

alloy. The probability of structural distortion is equivalent for all three (110) orientation. The atomic diagrams of distortion process are shown in Figure 2h–j. The distorted structures are transition state structures from 2H phase transform to 1T' phase. Those conclusion are further verified by epitaxially grown of up to three misaligned domains from a nucleation site in 1T' $\text{MoTe}_{2(1-x)}\text{S}_{2x}$ alloy (Figure S10, Supporting Information).

Different morphologies of monolayer $\text{MoTe}_{2(1-x)}\text{S}_{2x}$ alloys with continuously variable compositions (x from 0 to 1) have been obtained by systematically adjusting the mass ratio of S and Te powders during the growth process. The chemical composition and phase of each $\text{MoTe}_{2(1-x)}\text{S}_{2x}$ alloys are confirmed by XPS, Raman and photoluminescence (PL) spectra (Figures S11–13, Supporting Information). Figure 3a–e show ARPOM images of typical morphologies of monolayer $\text{MoTe}_{2(1-x)}\text{S}_{2x}$ alloys. The relationship between S/Te ratio and composition of $\text{MoTe}_{2(1-x)}\text{S}_{2x}$ alloys is shown in Figure S14 (Supporting Information). In $\text{MoTe}_{2(1-x)}\text{S}_{2x}$ synthesis, different S/Te ratios affect the morphology of alloys. According to our previous reported on, the growth rate is higher (010) orientation than along (100) orientation at 800 °C for 1T' MoTe_2 crystals, resulting in a ribbon-shape (Figure 3a).^[12] With the concentration of S increasing, the $\text{MoTe}_{1.84}\text{S}_{0.16}$ alloy exhibits branching shape with increased width

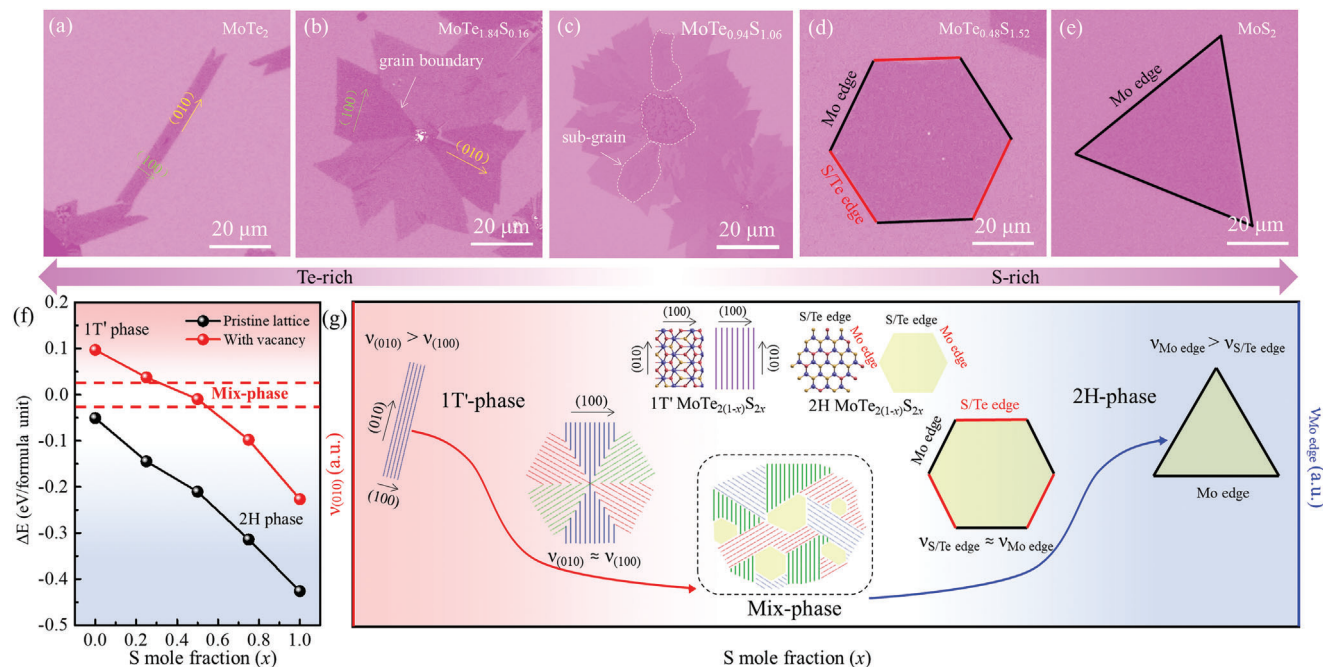


Figure 3. Growth mechanism of MoTe_{2(1-x)}S_{2x} alloys. a–e) OM images for 1T' MoTe₂, 1T' MoTe_{1.84}S_{0.16}, MoTe_{0.94}S_{1.06}, 2H MoTe_{0.48}S_{1.52}, 2H MoS₂, respectively. f) ΔE of the MoTe_{2(1-x)}S_{2x} monolayer as a function of S mole fraction (x). g) Mechanistic diagram of the evolution of morphology with composition associated with v₍₀₁₀₎ and v_{S/Te edge}.

(Figure 3b). The width-branching shape of MoTe_{1.84}S_{0.16} results from the decreased anisotropy of the crystal structure, which may cause the growth rate along both (010) and (100) orientation to be similar. The MoTe_{0.94}S_{1.06} alloy exhibits irregular shape due to the enriched nanoscale mix-phase structures (Figure 3c). AR-POM images at different polarization angles exhibit the disordered distribution of mix-phase (Figure S15, Supporting Information). To understand the composition-dependent phase stability and mix-phase formation in monolayer MoTe_{2(1-x)}S_{2x} alloys, we have conducted density-functional theory (DFT) calculations to identify the structural stability of 2H-phase and 1T'-phase MoTe_{2(1-x)}S_{2x} monolayers with varying S composition x from 0 to 1 (Figure 3f). The 2H-phase and 1T'-phase structures were investigated by using (2√3×3) and (2×3) supercells with the randomly distributed S and Te atoms (Figure S16, Supporting Information), respectively. Considering the lattice strain (≈2%) induced by the 2H-to-1T phase transition and lattice thermal vibration as well as the existence of chalcogenide vacancies, the strained 2H- and 1T'-phase models with a S (Te) vacancy is used to investigate the phase stability of monolayer MoTe_{2(1-x)}S_{2x} alloys. ΔE is the energy difference between the 2H and 1T' phases in each MoTe_{2(1-x)}S_{2x}, negative ΔE values mean that the 2H phase is more stable, and positive ΔE values suggest that the 1T' phase is energetically favorable. For the perfect MoTe_{2(1-x)}S_{2x} monolayers, the 2H phase is still more stable than the 1T' phase in all allowed compositions (Figure 3f). The result agrees well with the previous reports where 2H Mo-based dichalcogenides are energetically favorable.^[36–38] In contrast, the energy difference (ΔE) between the 2H and 1T' phases in the strained MoTe_{2(1-x)}S_{2x} monolayers with a S (or Te) vacancy gradually increases with de-

creasing composition x, as shown in Figure 3f. When the composition x is <0.5, the ΔE becomes positive values that means the 1T' phase will be energetically favorable. Therefore, high Te compositions contribute to the formation of 1T' MoTe_{2(1-x)}S_{2x}, which is consistent with our experimental observations in which Te-rich MoTe_{2(1-x)}S_{2x} nanostructures are dominated by 1T' phase. For the composition x located in the range of 0.3–0.5, the ΔE approaches 0 eV. This means that the thermodynamic stability of the 2H- and 1T'-phase MoTe_{2(1-x)}S_{2x} is largely similar, which triggered the growth of 2H/1T' mixed-phase as mentioned above.

As a result, the morphology of MoTe_{2(1-x)}S_{2x} alloys exhibits a regular evolution (ribbon-shape to width-branching, irregular shape, hexagonal and triangular) with respect to the chemical composition x (0 to 1) in Figure 3g. The supposed mechanism is that the hexagonal shape of the 2H MoTe_{0.48}S_{1.52} alloy may be attributed to the similar growth rates between S/Te-edge and Mo-edge (Figure 3d). Compared to grow monolayer MoTe_{0.48}S_{1.52}, the pressure of Te was reduced, which resulted in a higher growth rate on Mo-edge than S-edge, leading to a triangular finally (Figure 3e). This relationship between morphology and growth rate of S-edge/Mo-edge is typical 2H-phase TMDs.^[39,40] The established morphology-composition correlation provides a quick and efficient way to determine the approximate chemical composition of MoTe_{2(1-x)}S_{2x} alloy. Additionally, by controlling the volatilization time of S and Te powders, intriguing gear-like shape and heterojunction MoTe_{2(1-x)}S_{2x} alloys can be synthesized (Figure S17, Supporting Information).

The coherent atomic structures of enriched nanoscale mix-phase monolayer MoTe_{2(1-x)}S_{2x} alloys are further confirmed by large area Raman mapping. Figure 4a–c show high-resolution

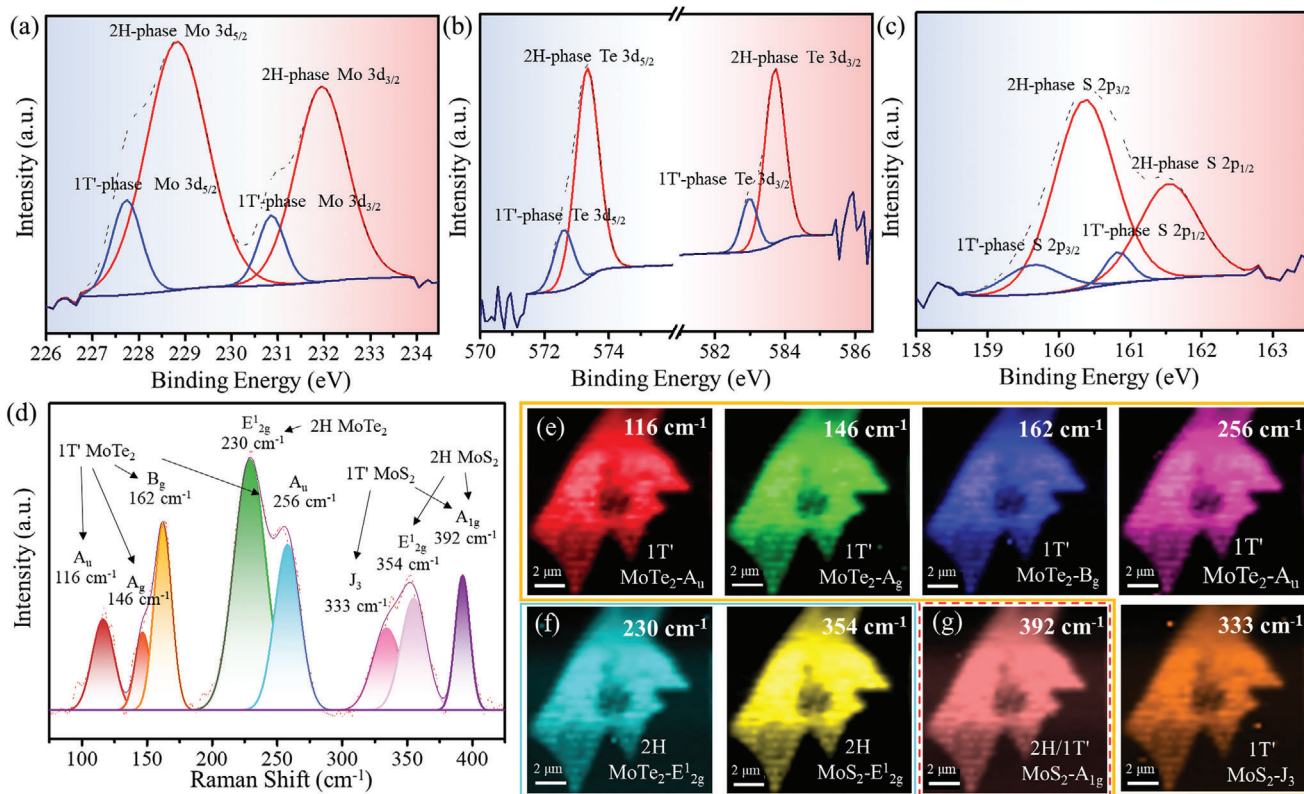


Figure 4. Characterization of the electronic structure of mix-phase $\text{MoTe}_{2(1-x)}\text{S}_{2x}$ alloy. a–c) High-resolution XPS spectra of Mo elements, Te elements, and S elements of mix-phase $\text{MoTe}_{2(1-x)}\text{S}_{2x}$ alloy, respectively. d) Raman single spectrum of mix-phase $\text{MoTe}_{2(1-x)}\text{S}_{2x}$ alloy. e, f) Raman mapping images of 1T' phase and 2H phase in mix-phase $\text{MoTe}_{2(1-x)}\text{S}_{2x}$ alloy, respectively. g) Raman mapping images at 392 cm^{-1} .

XPS spectra of Mo 3d, Te 3d, and S 2p of mix-phase $\text{MoTe}_{2(1-x)}\text{S}_{2x}$ alloys, respectively. Two doublets of core level peaks are present for Mo 3d, Te 3d, and S 2p spectra, attributed to two different electronic states around the same class of above atoms. In spectra of Mo 3d, 2H phase of peaks for Mo 3d_{5/2} and Mo 3d_{3/2} are located at 228.8 and 231.9 eV, while the 1T' phase are located at 227.7 and 230.8 eV (Figure 4a). As shown in Figure 4b, the peaks of Te 3d_{5/2} and Te 3d_{3/2} for 2H phase are located at 573.3 and 583.7 eV, while 1T' phase are located at 572.5 and 582.9 eV. The peaks of S 2p_{3/2} and S 2p_{1/2} for 2H phase are located at 160.4 and 161.5 eV, respectively, while the 1T' phase are located at 159.6 and 160.8 eV (Figure 4c). By calculating the peak area ratio of S to Te elements, the chemical composition of the mix-phase alloy is obtained as $\text{MoTe}_{0.94}\text{S}_{1.06}$. Further, mix-phase $\text{MoTe}_{2(1-x)}\text{S}_{2x}$ alloy in spatial distribution is analyzed by Raman mapping. The Raman spectra of mix-phase $\text{MoTe}_{2(1-x)}\text{S}_{2x}$ alloy derived from Raman mapping is shown in Figure 4d. During alloying, weakens and broadens the Raman peaks of mix-phase $\text{MoTe}_{2(1-x)}\text{S}_{2x}$ alloy is due to the softening or renormalization of phonon caused by the enhancement of electron–phonon coupling effect.^[41] Raman spectra exhibits typical peaks of 2H phase and 1T' phase mix-phase $\text{MoTe}_{2(1-x)}\text{S}_{2x}$ alloy. Figure 4e–g show Raman mapping images of different vibrational modes. In Figure 4e, the peaks observed at 116, 146, 162, 256, and 333 cm⁻¹ correspond to the vibration modes of 1T' $\text{MoTe}_2\text{-A}_u$ -like, 1T' $\text{MoTe}_2\text{-A}_g$ -like, 1T' $\text{MoTe}_2\text{-B}_g$ -like, 1T' $\text{MoTe}_2\text{-A}_u$ -like and 1T' $\text{MoS}_2\text{-J}_3$ -like, respectively. In Figure 4f, the peaks of 2H $\text{MoTe}_2\text{-E}^1_{2g}$ -like and 2H $\text{MoS}_2\text{-E}^1_{2g}$ -like are located at 230

and 354 cm⁻¹. The vibration modes of 1T' $\text{MoS}_2\text{-A}_{1g}$ -like and 2H $\text{MoS}_2\text{-A}_{1g}$ -like are located at the same wave number, so the peak at 392 cm⁻¹ could correspond to either the 1T' $\text{MoS}_2\text{-A}_{1g}$ -like or the 2H $\text{MoS}_2\text{-A}_{1g}$ -like (Figure 4g). The uniform distribution of peak intensity for Raman mapping at all vibration modes indicate that as-obtained monolayer $\text{MoTe}_{0.94}\text{S}_{1.06}$ alloys possess the presence of nanoscale 2H and 1T' phase in one domain with coherent atomic structure, and form the enriched nanoscale mix-phase finally.

To assess composition dependence of electrical transport and photodetection properties of monolayer $\text{MoTe}_{2(1-x)}\text{S}_{2x}$ alloys, we fabricated devices of alloys with different compositions on SiO_2/Si substrate. Take mix-phase $\text{MoTe}_{2(1-x)}\text{S}_{2x}$ alloys as an example, Figure S18 (Supporting Information) shows the structure and physical drawing of as-fabricated device. Figure S19 (Supporting Information) illustrates the output ($I_{ds}-V_{ds}$) and transfer ($I_{ds}-V_{gs}$) curves for pure 2H MoS_2 . The 2H MoS_2 device exhibits n-type conductive behavior with an electron mobility of $11.9\text{ cm}^2\text{V}^{-1}\text{s}^{-1}$. Figure 5a shows the output characteristic curves of the $\text{MoTe}_{0.48}\text{S}_{1.52}$ alloy device. The $I_{ds}-V_{ds}$ curves exhibit a linear relationship indicating that the source and drain electrodes form the good contact. The $I_{ds}-V_{gs}$ curves of monolayer $\text{MoTe}_{0.48}\text{S}_{1.52}$ alloy device exhibits bipolar behavior, where the electron mobility and hole mobility are 0.58 and $0.83\text{ cm}^2\text{V}^{-1}\text{s}^{-1}$, respectively (Figure 5b). The bipolar behavior results from the substitution of Te atoms at S sites, which increases the concentration of hole carriers (p-type doping).^[42,43] The relative low mobility for

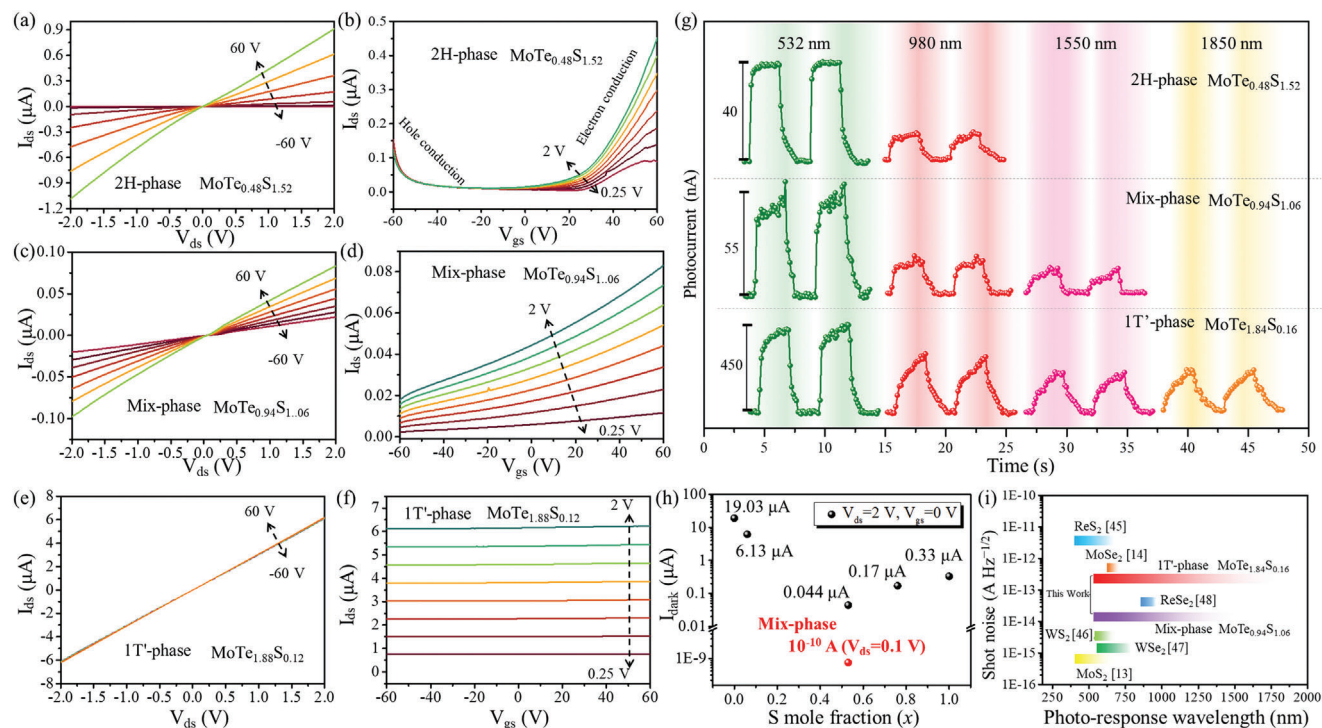


Figure 5. Electrical transport and photo-response properties of $\text{MoTe}_{2(1-x)}\text{S}_{2x}$ alloys. a,b) The output and transfer curves of the $\text{MoTe}_{0.48}\text{S}_{1.52}$ alloy, respectively. c,d) The output and transfer curves of mix-phase $\text{MoTe}_{0.94}\text{S}_{1.06}$ alloy, respectively. e,f) The output and transfer curves of the $\text{MoTe}_{1.88}\text{S}_{0.12}$ alloy, respectively. g) Photocurrent as a function of time of 2H $\text{MoTe}_{0.48}\text{S}_{1.52}$, 2H/1T' $\text{MoTe}_{0.94}\text{S}_{1.06}$, 1T' $\text{MoTe}_{1.88}\text{S}_{0.12}$ devices under light illumination with different wavelength of 532, 980, 1550, and 1850 nm. $V_{ds} = 2$ V, $V_{gs} = 0$ V. h) I_{dark} of $\text{MoTe}_{2(1-x)}\text{S}_{2x}$ alloys with compositions from 0 to 1. i) The comparable photo-response range and shot noise of various monolayer TMDs based photodetectors from reported works and this work.

$\text{MoTe}_{0.48}\text{S}_{1.52}$ alloy may be attributed to the increased alloy scattering and ionized impurity scattering in the sample, which is commonly observed in the group-VI TMDs alloys.^[44–48] For mix-phase $\text{MoTe}_{0.94}\text{S}_{1.06}$ devices, the effect of gate voltage on current modulation is significantly weaker. For $I_{\text{ds}}-V_{\text{ds}}$ curves as shown in Figure 5c, the gate voltage (-60 V to 60 V) only modulates the current from 22 nA to 83 nA with $V_{\text{ds}} = 2$ V. For the $I_{\text{ds}}-V_{\text{gs}}$ curves, the device still exhibits n-type conductive behavior even though it can no longer achieve effective on/off (Figure 5d). By increasing the concentration of Te ($x = 0.06$), the device exhibits a semi-metallic conductivity behavior that is independent of gate voltage (Figure 5e,f). Figure S20 (Supporting Information) shows the output and transfer curves of pure 1T' MoTe_2 , which exhibit the semi-metallic conductivity behavior. The composition x of $\text{MoTe}_{2(1-x)}\text{S}_{2x}$ alloy from 1 to 0 achieved the modulation of the conductive behavior from n-type to bipolar and semi-metal.

For the photodetection performance, pure 2H MoS_2 monolayer can only respond the light of 532 nm, the dark current (I_{dark}) is ≈ 0.33 μA , and the rise (τ_{rise}) and decay times (τ_{decay}) of photocurrent are 33 and 78 ms, respectively (Figure S21, Supporting Information). The pure 1T' MoTe_2 -based photodetector has a broadband response from 532 to 1850 nm, and the I_{dark} is around as high as 19.03 μA due to the zero-bandgap structure of semi-metal, and the rise and decay times of the photocurrent are 5.8 and 3.2 s, respectively (Figure S22, Supporting Information). Figure 5g shows the photo-response properties of $\text{MoTe}_{2(1-x)}\text{S}_{2x}$ alloy devices measured under light irradiation with different

wavelengths. $\text{MoTe}_{0.48}\text{S}_{1.52}$ alloy with pure 2H phase only broadens the response wavelength range to 980 nm, while mix-phase $\text{MoTe}_{0.94}\text{S}_{1.06}$ alloy exhibits significant wide wavelength range from 532 to 1550 nm. The zero-bandgap structure of the 1T' phase in mix-phase $\text{MoTe}_{0.94}\text{S}_{1.06}$ alloy generates photogenerated carriers, which broaden the response wavelength range. 1T' $\text{MoTe}_{1.88}\text{S}_{0.12}$ exhibits the same response wavelength range (532 – 1850 nm) as pure 1T' MoTe_2 . Specially, Figure 5h shows the dark currents for different compositions of $\text{MoTe}_{2(1-x)}\text{S}_{2x}$ alloy at V_{ds} of 2 V and V_{gs} of 0 V. The I_{dark} of $\text{MoTe}_{2(1-x)}\text{S}_{2x}$ -based devices exhibits a decreasing and then increasing trend with chemical composition x (0 – 1). The mix-phase $\text{MoTe}_{0.94}\text{S}_{1.06}$ alloy exhibits the lowest I_{dark} of 10^{-10} A at 100 mV. For mix-phase $\text{MoTe}_{2(1-x)}\text{S}_{2x}$ alloys, the increased interface scattering and ionized impurity scattering should be main factors to reduce the I_{dark} due to the coherent phase interfaces crystal structure. What's more, the barriers of energy level at the coherent phase interfaces may also further inhibit the inner layer carrier transport, which may also further reduce I_{dark} . In addition, Figure S23 (Supporting Information) shows the response time for $\text{MoTe}_{2(1-x)}\text{S}_{2x}$ alloys with composition from 1 to 0 under 532 nm illumination. The τ_{rise} and τ_{decay} of 2H $\text{MoTe}_{0.48}\text{S}_{1.52}$ are 81 and 250 ms, respectively. The τ_{rise} and τ_{decay} of mix-phase $\text{MoTe}_{0.94}\text{S}_{1.06}$ are 258 and 550 ms, respectively. The τ_{rise} and τ_{decay} of 1T' $\text{MoTe}_{1.88}\text{S}_{0.12}$ are 1.28 and 1.13 s, respectively. The decrease in response time is caused by the increased 1T' phase alloy component. Table S1 (Supporting Information) shows the photo-response of $\text{MoTe}_{2(1-x)}\text{S}_{2x}$ -based

($0 \leq x \leq 1$) devices. Among them, the responsivity of monolayer mix-phase $\text{MoTe}_{0.94}\text{S}_{1.06}$ alloys at 532, 980, and 1550 nm is $\approx 230, 110, \text{ and } 101 \text{ mA W}^{-1}$, respectively. Here, responsivity (R) is defined as $R = (I_{\text{light}} - I_{\text{dark}})/P$, where I_{light} and I_{dark} are currents measured under light irradiation and dark states, respectively, and P is the applied light power onto devices. The comparable data of shot noise and photo-response wavelength toward pure monolayer TMDs-based photodetectors are shown in Figure 5i. Among them, the equivalent dark current shot noise, can be calculated as, $\sqrt{2eI_{\text{dark}}}$.^[49] The short noise of mix-phase $\text{MoTe}_{0.94}\text{S}_{1.06}$ alloy is $\approx 10^{-14} \text{ A Hz}^{-1/2}$, which is much lower than that of 1T' $\text{MoTe}_{1.88}\text{S}_{0.12}$ alloy. The results demonstrated that the mix-phase $\text{MoTe}_{2(1-x)}\text{S}_{2x}$ alloy with coherent phase interfaces shown acceptable short noise while broadening the photo-response wavelength range with low dark current at same time for pure TMDs.

3. Conclusion

In summary, we synthesized enriched nanoscale mix-phase $\text{MoTe}_{2(1-x)}\text{S}_{2x}$ alloy with coherent atomic structures by composition-triggered growth for broadband photodetection. The XPS, Raman mapping, and ARPOM characterization of large-area mix-phase alloys demonstrate enriched nanoscale mix-phase structures. The DFT calculation of composition-dependent formation energies indicates that similar chemical compositions of S/Te atoms are crucial to triggering the growth of mix-phase alloys. The transition states of coherent atomic structure from 2H to 1T' phase are discovered in mix-phase $\text{MoTe}_{2(1-x)}\text{S}_{2x}$ alloy by STEM. Electrical transport and photo-response measurements reveal that mix-phase $\text{MoTe}_{2(1-x)}\text{S}_{2x}$ alloy exhibits n-type electrical transport behavior and a broadband photo-response from 532 to 1550 nm with dark current $\approx 10^{-10} \text{ A}$ at 100 mV bias voltage. Our study fully exploits the advantages of the 2H and 1T' phases, providing an effective strategy for pure TMDs to achieve high performance broadband photodetectors.

4. Experimental Section

Synthesis of $\text{MoTe}_{2(1-x)}\text{S}_{2x}$: Sulfur (S) and tellurium (Te) powders were placed into two quartz boats at the temperature of $T_{\text{S}} \approx 200 \text{ }^\circ\text{C}$ and $T_{\text{Te}} \approx 500 \text{ }^\circ\text{C}$, respectively. The amount of Te was fixed at 80 mg, while the amount of S was adjusted from 1 to 80 mg. A ceramic boat loaded with the mixture of MoO_3 powder and NaCl were placed at the heating center of a quartz tube, and Si/SiO₂ substrate was put on the boat with the polishing surface down. Note that the mixtures of MoO_3 and NaCl were covered by a layer of molecular sieve, which could restrict the volatilization rate of Mo sources, and thus benefit to control the growth kinetics for obtaining alloys with uniform composition and phase structure. A mixture of Ar (20 sccm) and H₂ (10 sccm) was used as the carrier gas throughout the whole process. The reaction temperature was set at 800 °C with a ramping rate of 30 °C min⁻¹ and maintained for 10 min for the growth of $\text{MoTe}_{2(1-x)}\text{S}_{2x}$.

Structure and Composition Characterization: ARPOM images were taken on an Olympus BX51 microscope. AFM images were done on a Bruker Dimension Icon microscope. SEM characterization was measured with FEI Verios G4. XPS analysis was done on an Axis Ultra system. Raman spectra were measured by WITec in Alpha300R with 532 nm laser.

Device Fabrication and Electrical Measurement: The monolayer $\text{MoTe}_{2(1-x)}\text{S}_{2x}$ crystal devices were fabricated on SiO₂/Si with the thickness of oxide layer $\approx 300 \text{ nm}$ by electron-beam lithography and physical

mask with Cu grid, and the contact metal of Cr/Au (10/50 nm) electrodes were fabricated by thermal evaporation deposition. The electrical characteristics measurement was carried out in a probe station and measured by Keithley 2614b semiconductor analyzer under ambient air at room temperature. The charge-transport behaviors of the as-fabricated devices were measured at room temperature (300 K). Wavelength-dependent photo-response of the devices were performed under the 532, 950, 1550, and 1850 nm laser.

Density-Functional Theory Calculations: All DFT calculations were performed by using the projector augmented wave (PAW) method as implemented in the Vienna ab initio Simulation Package (VASP).^[50,51] The generalized-gradient approximation (GGA) functional in the form of Perdew–Burke–Ernzerh (PBE) was used to treat the electronic exchange–correlation energy.^[52] A kinetic energy cutoff was set to 500 eV for the plane-wave expansion set. The Monkhorst–Pack scheme was used for the k -point sampling in the Brillouin zone with the grid of $6 \times 6 \times 1$ for monolayer $\text{MoTe}_{2(1-x)}\text{S}_{2x}$ alloys. A vacuum layer of $> 15 \text{ \AA}$ along the out-of-plane direction was introduced into the unit cell of $\text{MoTe}_{2(1-x)}\text{S}_{2x}$ monolayers to avoid the interactions between adjacent periodic slabs. The geometric optimization was performed using the conjugate-gradient method, and the convergence criteria of energy and force were set to $10^{-4} \text{ eV atom}^{-1}$ and $10^{-2} \text{ eV \AA}^{-1}$, respectively.

Supporting Information

Supporting Information is available from the Wiley Online Library or from the author.

Acknowledgements

X.W. and M.Z. contributed equally to this work. This work was supported by the National Key Research and Development Program of China (2021YFA0717600), the National Natural Science Foundation of China (52272163, 62022081, 61974099, and 62174151), and Fundamental Research Funds for the Central Universities (D5000230122). Computational resources from the HZWTECH are acknowledged.

Conflict of Interest

The authors declare no conflict of interest.

Data Availability Statement

The data that support the findings of this study are available in the supplementary material of this article.

Keywords

broadband photodetectors, formation energy, mix-phase, $\text{MoTe}_{2(1-x)}\text{S}_{2x}$ alloy, photo-response range

Received: August 23, 2023
Revised: October 3, 2023
Published online: November 2, 2023

- [1] S. Yuan, D. Naveh, K. Watanabe, T. Taniguchi, F. Xia, *Nat. Photonics* **2021**, *15*, 601.
- [2] H. Lin, B. C. P. Sturmberg, K.-T. Lin, Y. Yang, X. Zheng, T. K. Chong, C. M. De Sterke, B. Jia, *Nat. Photonics* **2019**, *13*, 270.

- [3] H. Yua, X. Liu, F. Afshinmanesh, W. Li, G. Xu, J. Sun, B. Lian, A. G. Curto, G. Ye, Y. Hikita, Z. Shen, S.-C. Zhang, X. Chen, M. Brongersma, H. Y. Hwang, Y. Cui, *Nat. Nanotechnol.* **2015**, *10*, 707.
- [4] S. Du, W. Lu, A. Ali, P. Zhao, K. Shehzad, H. Guo, L. Ma, X. Liu, X. Pi, P. Wang, H. Fang, Z. Xu, C. Gao, Y. Dan, P. Tan, H. Wang, C.-T. Lin, J. Yang, S. Dong, Z. Cheng, E. Li, W. Yin, J. Luo, B. Yu, T. Hasan, Y. Xu, W. Hu, X. Duan, *Adv. Mater.* **2017**, *29*, 1700463.
- [5] V. Krishnamurthi, H. Khan, T. Ahmed, A. Zavabeti, S. A. Tawfik, S. K. Jain, M. J. S. Spencer, S. Balendhran, K. B. Crozier, Z. Li, L. Fu, M. Mohiuddin, M. X. Low, B. Shabbir, A. Boes, A. Mitchell, C. F. Mcconville, Y. Li, K. Kalantar-Zadeh, N. Mahmood, S. Walia, *Adv. Mater.* **2020**, *32*, 2004247.
- [6] W. Hu, X. Chen, Z. Ye, W. Lu, *Appl. Phys. Lett.* **2011**, *99*, 091110.
- [7] R. Maiti, C. Patil, M. A. S. R. Saadi, T. Xie, J. G. Azadani, B. Uluutku, R. Amin, A. F. Briggs, M. Miscuglio, D. Van Thourhout, S. D. Solares, T. Low, R. Agarwal, S. R. Bank, V. J. Sorger, *Nat. Photonics* **2020**, *14*, 578.
- [8] A. Dodda, A. Oberoi, A. Sebastian, T. H. Choudhury, J. M. Redwing, S. Das, *Nat. Commun.* **2020**, *11*, 4406.
- [9] Y.-Q. Bie, G. Grosso, M. Heuck, M. M. Furchi, Y. Cao, J. Zheng, D. Bunandar, E. Navarro-Moratalla, L. Zhou, D. K. Efetov, T. Taniguchi, K. Watanabe, J. Kong, D. Englund, P. Jarillo-Herrero, *Nat. Nanotechnol.* **2017**, *12*, 1124.
- [10] X. Yang, X. Zhou, L. Li, N. Wang, R. Hao, Y. Zhou, H. Xu, Y. Li, G. Zhu, Z. Zhang, J. Wang, Q. Feng, *Small* **2023**, *19*, 2206590.
- [11] T. Zhao, J. Guo, T. Li, Z. Wang, M. Peng, F. Zhong, Y. Chen, Y. Yu, T. Xu, R. Xie, P. Gao, X. Wang, W. Hu, *Chem. Soc. Rev.* **2023**, *52*, 1650.
- [12] X. Chen, G. Liu, W. Zheng, W. Feng, W. Cao, W. Hu, P. Hu, *Adv. Funct. Mater.* **2016**, *26*, 8537.
- [13] O. Lopez-Sanchez, D. Lembke, M. Kayci, A. Radenovic, A. Kis, *Nat. Nanotechnol.* **2013**, *8*, 497.
- [14] W. Zhang, M.-H. Chiu, C.-H. Chen, W. Chen, L.-J. Li, A. T. S. Wee, *ACS Nano* **2014**, *8*, 8653.
- [15] X. Wang, J. Shang, M. Zhu, X. Zhou, R. Hao, L. Sun, H. Xu, J. Zheng, X. Lei, C. Li, L. Kou, Q. Feng, *Nanoscale Horiz.* **2020**, *5*, 954.
- [16] C. H. Lee, Y. Park, S. Youn, M. J. Yeom, H. S. Kum, J. Chang, J. Heo, G. Yoo, *Adv. Funct. Mater.* **2022**, *32*, 2107992.
- [17] L.-H. Zeng, S.-H. Lin, Z.-J. Li, Z.-X. Zhang, T.-F. Zhang, C. Xie, C.-H. Mak, Y. Chai, S. P. Lau, L.-B. Luo, Y. H. Tsang, *Adv. Funct. Mater.* **2018**, *28*, 1705970.
- [18] S. Ghosh, W. C. Chiang, M. Y. Fakhri, C. T. Wu, R. S. Chen, S. Chattopadhyay, *Nano Energy* **2020**, *67*, 104258.
- [19] Q. Deng, X. Li, H. Si, J. Hong, S. Wang, Q. Feng, C.-X. Hu, S. Wang, H.-L. Zhang, K. Suenaga, H. Xu, *Adv. Funct. Mater.* **2020**, *30*, 2003264.
- [20] S. Zhang, Y. Wu, F. Gao, H. Shang, J. Zhang, Z. Li, Y. Fu, P. Hu, *Adv. Funct. Mater.* **2022**, *32*, 2205299.
- [21] Z. Lu, Y. Xu, Y. Yu, K. Xu, J. Mao, G. Xu, Y. Ma, D. Wu, J. Jie, *Adv. Funct. Mater.* **2020**, *30*, 1907951.
- [22] X. Wang, H. Shen, Y. Chen, G. Wu, P. Wang, H. Xia, T. Lin, P. Zhou, W. Hu, X. Meng, J. Chu, J. Wang, *Adv. Sci.* **2019**, *6*, 1901050.
- [23] X. Wang, P. Wang, J. Wang, W. Hu, X. Zhou, N. Guo, H. Huang, S. Sun, H. Shen, T. Lin, M. Tang, L. Liao, A. Jiang, J. Sun, X. Meng, X. Chen, W. Lu, J. Chu, *Adv. Mater.* **2015**, *27*, 6575.
- [24] Z. Zhang, Z. Huang, J. Li, D. Wang, Y. Lin, X. Yang, H. Liu, S. Liu, Y. Wang, B. Li, X. Duan, X. Duan, *Nat. Nanotechnol.* **2022**, *17*, 493.
- [25] Z. Huang, A. Alharbi, W. Mayer, E. Cuniberto, T. Taniguchi, K. Watanabe, J. Shabani, D. Shahrjerdi, *Nat. Commun.* **2020**, *11*, 302.
- [26] D. G. Purdie, N. M. Pugno, T. Taniguchi, K. Watanabe, A. C. Ferrari, A. Lombardo, *Nat. Commun.* **2018**, *9*, 5387.
- [27] H. Li, Q. Zhang, X. Duan, X. Wu, X. Fan, X. Zhu, X. Zhuang, W. Hu, H. Zhou, A. Pan, X. Duan, *J. Am. Chem. Soc.* **2015**, *137*, 5284.
- [28] Y. Chen, J. Xi, D. O. Dumcenco, Z. Liu, K. Suenaga, D. Wang, Z. Shuai, Y.-S. Huang, L. Xie, *ACS Nano* **2013**, *7*, 4610.
- [29] F. Cui, Q. Feng, J. Hong, R. Wang, Y. Bai, X. Li, D. Liu, Y. Zhou, X. Liang, X. He, Z. Zhang, S. Liu, Z. Lei, Z. Liu, T. Zhai, H. Xu, *Adv. Mater.* **2017**, *29*, 1705015.
- [30] P. Yu, J. Lin, L. Sun, Q. L. Le, X. Yu, G. Gao, C.-H. Hsu, D. Wu, T.-R. Chang, Q. Zeng, F. Liu, Q. J. Wang, H.-T. Jeng, H. Lin, A. Trampert, Z. Shen, K. Suenaga, Z. Liu, *Adv. Mater.* **2017**, *29*, 1603991.
- [31] Q. Feng, Y. Zhu, J. Hong, M. Zhang, W. Duan, N. Mao, J. Wu, H. Xu, F. Dong, F. Lin, C. Jin, C. Wang, J. Zhang, L. Xie, *Adv. Mater.* **2014**, *26*, 2648.
- [32] Q. Feng, N. Mao, J. Wu, H. Xu, C. Wang, J. Zhang, L. Xie, *ACS Nano* **2015**, *9*, 7450.
- [33] B. Tang, J. Zhou, P. Sun, X. Wang, L. Bai, J. Dan, J. Yang, K. Zhou, X. Zhao, S. J. Pennycook, Z. Liu, *Adv. Mater.* **2019**, *31*, 1900862.
- [34] M. Zhu, Y. Zhao, Q. Feng, H. Lu, S. Zhang, N. Zhang, C. Ma, J. Li, J. Zheng, J. Zhang, H. Xu, T. Zhai, J. Zhao, *Small* **2019**, *15*, 1903159.
- [35] X. Li, X. Wang, J. Hong, D. Liu, Q. Feng, Z. Lei, K. Liu, F. Ding, H. Xu, *Adv. Funct. Mater.* **2019**, *29*, 1906385.
- [36] K. N. Duerloo, Y. Li, E. J. Reed, *Nat. Comm.* **2014**, *5*, 4214.
- [37] X. Zhou, H. Shu, Q. Li, P. Liang, D. Cao, X. Chen, *J. Mater. Chem. C* **2020**, *8*, 4432.
- [38] W. Li, X. Qian, J. Li, *Nat. Rev. Mater.* **2021**, *6*, 829.
- [39] V. T. Vu, T. T. H. Vu, T. L. Phan, W. T. Kang, Y. R. Kim, M. D. Tran, H. T. T. Nguyen, Y. H. Lee, W. J. Yu, *ACS Nano* **2021**, *15*, 13031.
- [40] S. Wang, Y. Rong, Y. Fan, M. Pacios, H. Bhaskaran, K. He, J. H. Warner, *Chem. Mater.* **2014**, *26*, 6371.
- [41] S. Susarla, A. Kutana, J. A. Hachtel, V. Kochat, A. Apte, R. Vajtai, J. C. Idrobo, B. I. Yakobson, C. S. Tiwary, P. M. Ajayan, *Adv. Mater.* **2017**, *29*, 1702457.
- [42] S. J. Yun, G. H. Han, H. Kim, D. L. Duong, B. G. Shin, J. Zhao, Q. A. Vu, J. Lee, S. M. Lee, Y. H. Lee, *Nat. Commun.* **2017**, *8*, 2163.
- [43] D. H. Keum, S. Cho, J. H. Kim, D.-H. Choe, H.-J. Sung, M. Kan, H. Kang, J.-Y. Hwang, S. W. Kim, H. Yang, K. J. Chang, Y. H. Lee, *Nat. Phys.* **2015**, *11*, 482.
- [44] X. Duan, C. Wang, Z. Fan, G. Hao, L. Kou, U. Halim, H. Li, X. Wu, Y. Wang, J. Jiang, A. Pan, Y. Huang, R. Yu, X. Duan, *Nano Lett.* **2016**, *16*, 264.
- [45] J. Shim, A. Oh, D.-H. Kang, S. Oh, S. K. Jang, J. Jeon, M. H. Jeon, M. Kim, C. Choi, J. Lee, S. Lee, G. Y. Yeom, Y. J. Song, J.-H. Park, *Adv. Mater.* **2016**, *28*, 6985.
- [46] Q. Wang, Q. Zhang, X. Zhao, Y. J. Zheng, J. Wang, X. Luo, J. Dan, R. Zhu, Q. Liang, L. Zhang, P. K. J. Wong, X. He, Y. L. Huang, X. Wang, S. J. Pennycook, G. Eda, A. T. S. Wee, *Nano Lett.* **2019**, *19*, 5595.
- [47] Y.-H. Chang, W. Zhang, Y. Zhu, Y. Han, J. Pu, J.-K. Chang, W.-T. Hsu, J.-K. Huang, C.-L. Hsu, M.-H. Chiu, T. Takenobu, H. Li, C.-I. Wu, W.-H. Chang, A. T. S. Wee, L.-J. Li, *ACS Nano* **2014**, *8*, 8582.
- [48] F. Cui, X. Li, Q. Feng, J. Yin, L. Zhou, D. Liu, K. Liu, X. He, X. Liang, S. Liu, Z. Lei, Z. Liu, H. Peng, J. Zhang, J. Kong, H. Xu, *Nano Res.* **2017**, *10*, 2732.
- [49] D. Zheng, H. Fang, M. Long, F. Wu, P. Wang, F. Gong, X. Wu, J. C. Ho, L. Liao, W. Hu, *ACS Nano* **2018**, *12*, 7239.
- [50] P. E. Blöchl, *Phys. Rev. B* **1994**, *50*, 17953.
- [51] G. Kresse, J. Furthmüller, *Phys. Rev. B* **1996**, *54*, 11169.
- [52] M. C. Payne, M. P. Teter, D. C. Allan, T. A. Arias, J. D. Joannopoulos, *Rev. Mod. Phys.* **1992**, *64*, 1045.